Inorganic Chemistry

Article

pubs.acs.org/IC

Hypoxia-Responsive ^{19}F MRI Probes with Improved Redox Properties and Biocompatibility

Da Xie,[†] Seyong Kim,[†] Vikraant Kohli,[†] Arnab Banerjee,[†] Meng Yu,[†] José S. Enriquez,[†] Jeffrey J. Luci,[‡,§] and Emily L. Que*[,†]

[†]Department of Chemistry, The University of Texas at Austin, 105 E. 24th Street Stop A5300, Austin, Texas 78712, United States

[‡]Department of Neuroscience, The University of Texas at Austin, Austin, Texas 78712, United States

[§]Imaging Research Center, The University of Texas at Austin, Austin, Texas 78712, United States

Supporting Information

ABSTRACT: ^{19}F magnetic resonance imaging (MRI), an emerging modality in biomedical imaging, has shown promise for in vitro and in vivo preclinical studies. Here we present a series of fluorinated Cu(II)ATSM derivatives for potential use as ^{19}F magnetic resonance agents for sensing cellular hypoxia. The synthesized complexes feature a hypoxia-targeting Cu^{2+} coordination core, nine equivalent fluorine atoms connected via a variable-length poly(ethylene glycol) linker. Introduction of the fluorine moiety maintains the planar coordination geometry of the Cu^{2+} center, while the linker length modulates the $Cu^{2+/+}$ reduction potential, ^{19}F NMR relaxation properties, and lipophilicity. In particular, the ^{19}F NMR relaxation properties were quantitatively evaluated by the Solomon−Bloembergen model, revealing a regular pattern of relaxation enhancement tuned by the distance between Cu^{2+} and F atoms. Finally, the potential utility of these complexes for sensing reductive environments was demonstrated using both ^{19}F MR phantom imaging and ^{19}F NMR, including experiments in intact live cells.

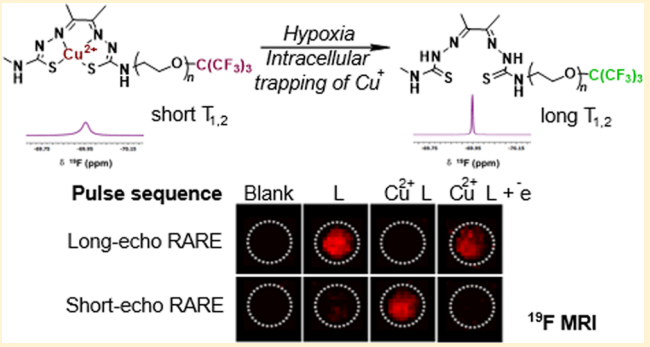

1. INTRODUCTION

Hypoxia (oxygen deficiency) is a downstream effect of accelerated cellular events such as proliferation, or an inadequate vasculature to supply oxygen due to disease and/or aberrant physiological environments. Hypoxia can lead to severe pathologies including genetic instability and malignant progression of cells.[1−4] Decreased oxygen levels have been observed in a number of different types of cancer, ranging from brain to subcutis, compared to normal tissue or organs.[5] Indeed, hypoxia represents an essential prognostic marker, and its identification is important for planning cancer treatment.[1−4] To date, multiple imaging modalities have been utilized for detecting cellular hypoxia, including magnetic resonance imaging (MRI),[5−18] luminescence imaging,[19−21] and positron emission tomography (PET).[22,23] Among them, an MRI-based approach is clinically desirable and practical, since it enables whole-body imaging with high spatial resolution and anatomic detail without exposing subjects to ionizing radiation. A number of responsive contrast agents have been pursued for sensing hypoxia through MR-based approaches including ^{1}H,[6−9] ^{19}F,[10−12] ^{31}P,[13] and hyperpolarized NMR[14−16]-based probes.

^{19}F MRI, owing to the favorable MR properties of the ^{19}F nucleus and negligible ^{19}F signal in the human body, has shown promise in complementing the wealth of information provided by ^{1}H MRI.[12,24−26] In particular, use of superfluorinated molecules such as perfluorocarbons (PFCs) and perfluoropolyethers (PFPE) has found success for in vivo cell tracking and measurement of tumor oxygenation through ^{19}F MRI.[12,27−29] Inorganic scaffolds containing paramagnetic metal ions have proven to be powerful for use as sensing platforms for MRI.[30−49] In the context of ^{19}F MRI, paramagnetic metal centers shorten the relaxation times of nearby fluorine nuclei, and these have been used to develop responsive ^{19}F MR imaging agents based on the modulation of T_2 (transverse relaxation time) of ^{19}F.[38,39,50] More importantly, judicious choice of the paramagnetic metals for a fluorinated system with short T_1 (longitudinal relaxation time) and a T_2/T_1 ratio close to unity enables more rapid acquisition of MR signals, thus achieving a high signal-to-noise ratio within a certain acquisition time to help overcome the intrinsic sensitivity challenge of ^{19}F MRI.[51−54] Recently, this has been demonstrated in a fluorinated nanoemulson incorporated with a high-spin Fe(III) center, enabling sensitive cellular ^{19}F MRI in vivo.[55]

Previously, we demonstrated the use of a ^{19}F MR-based approach to differentiate cells grown in hypoxic versus normoxic environments. Our first generation probe was based

Received: February 26, 2017

DOI: 10.1021/acs.inorgchem.7b00500
Inorg. Chem. XXXX, XXX, XXX−XXX

on a trifluorinated Cu(II)ATSM complex (Cu(II)ATSM-F_3, ATSM = diacetyl-bis(4-methylthiosemicarbazonato)).[50] Cu^{2+} possesses a relatively long longitudinal electronic relaxation time (T_{1e}), on the scale of 10^{-8} to 10^{-10} seconds, largely due to its well-separated electronic excited states.[56−58] This property significantly shortens the T_2 values of interacting ^{19}F nuclei,[59] such that no fluorine signal is observed in Cu(II)ATSM-F_3. In hypoxic environments, the reduction of Cu^{2+} to Cu^{+} and ligand dissociation affords the related diamagnetic $[Cu(I)ATSM\text{-}F_3]^-$ complex and free ligand, effectively lengthening the T_2 and restoring a robust ^{19}F signal.

As a proof-of-concept system, Cu(II)ATSM-F_3 nicely demonstrated that one-electron redox changes that convert an $S = {}^1/_2$ system to an $S = 0$ system can be exploited for developing redox sensors for ^{19}F MRI. CuATSM-based complexes display a well-studied relationship between reduction potential and selectivity toward hypoxic regions, and their redox properties are readily controlled by the ligand.[60] In addition, CuATSM derivatives have the advantage of being cell-permeable, which enables the interrogation of the intracellular milieu. In this paper, we report a series of new fluorinated CuATSM derivatives (**Cu1−4**, Scheme 1) containing higher fluorine density and modified redox and relaxation properties through the introduction of a variable-length linker in efforts to improve sensitivity and selectivity of this class of probes. In these complexes, the fluorine nuclei are further from the paramagnetic Cu^{2+} relative to our previous complexes, resulting in ^{19}F relaxation times that are attenuated yet NMR and MRI signals that are not fully quenched. By taking **Cu4** and its ligand, **4**, as representative compounds, we collected ^{19}F MR phantom images that demonstrate selective imaging of the complex versus the ligand through different ^{19}F MR pulse sequences with a detection limit of 0.44 mM for **4** and 0.099 mM for **Cu4** and demonstrated the use of **Cu4** for ^{19}F NMR-based differentiation of hypoxic cells versus normoxic cells in live, whole cell experiments.

Scheme 1. Structure of Complexes Cu1-4

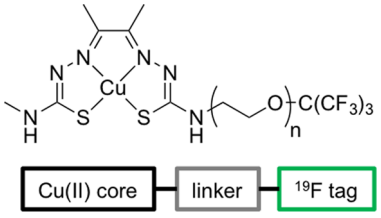

CuATSM-peg$_n$-F_9 (n = 1, 2, 3, 4), **Cu1-4**

2. RESULTS AND DISCUSSION

2.1. Synthesis. Synthesis of CuATSM derivatives **Cu1−4** was carried out starting from 4-methylsemicarbozone (Scheme 2). Two-step imine condensation afforded the ligand precursor in 69% yield. Refluxing the ligand precursor with fluorinated amines containing different ethylene glycol chain lengths provided the ligands, **1−4**, in 59−82% yield.[61] Final coordination was achieved using Cu(II) acetate in high yield (82−90%), and the resulting complexes **Cu1−4** were purified using reverse-phase chromatography using acetonitrile and water as eluents. Complex purity was supported by high-resolution LC−MS, revealing the formation of 1:1 metal/ligand complexes.

2.2. Structural Characterization. Single crystals of **Cu1** were grown by slow evaporation of a concentrated toluene solution of the complex. The single crystal X-ray structure and important structural parameters are presented in Figure 1 and Tables S2−S4. In this complex, the Cu^{2+} sits in a pseudo-square-planar $[N_2S_2]$ pocket, and no intra- or intermolecular interactions are observed between the metal center and the ligand ether oxygen. The geometry of the Cu^{2+} coordination site well mimics the parent CuATSM complex, indicating a

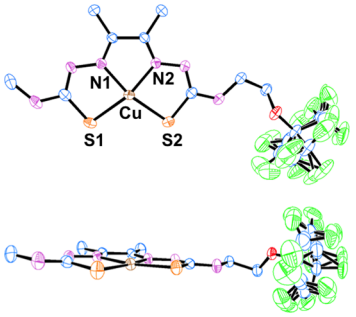

Figure 1. Molecular structure of **Cu1** from single crystal X-ray diffraction (top, top view; bottom, front view). Thermal ellipsoid plot at 50% probability level refined by a two-component disorder model. Solvent molecules and hydrogen atoms omitted for clarity.

Scheme 2. Synthesis of Cu1−4[a]

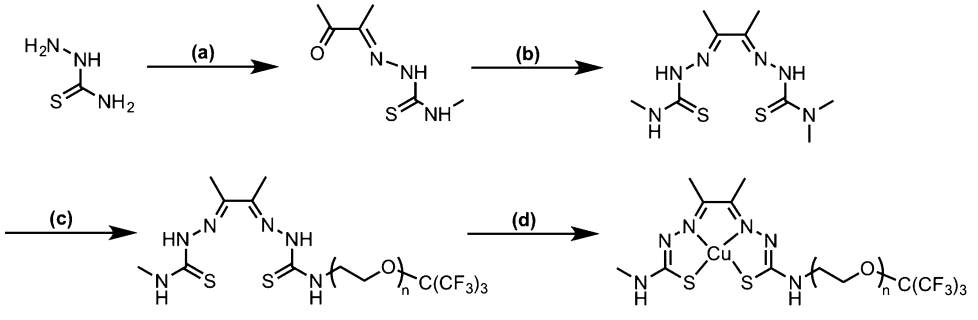

H_2ATSM-peg$_n$-F_9, **1-4** (n=1,2,3,4)

CuATSM-peg$_n$-F_9, **Cu1-4** (n=1,2,3,4)

[a]Conditions: (a) 2,3-butanedione, conc HCl, H_2O, 0−5 °C, 2.5 h (95%); (b) 4,4-dimethylsemicarbazone, acetic acid, DMF, room temperature (rt), 48 h (73%); (c) $H_2N(CH_2CH_2O)_nC(CF_3)_3$ (n = 1, 2, 3, 4), CH_3CN, 90 °C, 16 h (59−82%); (d) cupric acetate hydrate, DMF, rt, 16 h (82-90%).

DOI: 10.1021/acs.inorgchem.7b00500
Inorg. Chem. XXXX, XXX, XXX−XXX

similar chemical environment of the Cu^{2+}.[62] The average Cu^{2+}–F distance is 8.87 Å, longer than in first generation compounds CuATSM-F_3 (6.48 Å) and CuATSM-F_6, (6.66 Å).[50] Likely due to the flexible nature of the extended ethylene glycol linkers, single crystals of **Cu2**–**4** did not form.

Optimized structures of **Cu1**–**4** were obtained using density functional theory (DFT) calculations at the uB3LYP/6-31G(d,p) level (Figure S2). The optimized structure of **Cu1** well resembles its single crystal structure, and all four complexes share the same square planar coordination configuration. As expected, extending the ethylene glycol chain increases the distance between the paramagnetic Cu^{2+} center and the fluorine tags, with average Cu–F distances in **Cu1**–**4** of 8.98, 11.74, 15.12, and 18.18 Å, respectively. The above results suggest analogous coordination environments of Cu^{2+} in **Cu1**–**4** and CuATSM, and no interactions were observed between the oxygen atoms contained in the linker and Cu(II).

2.3. EPR Spectroscopy. EPR spectra for all four complexes were recorded in DMF at room temperature (Figure 2). **Cu1**–**4** displayed nearly identical EPR spectra at room temperature, with g_{iso} = 2.062 and A_{Cu} = 97 G. These values fall well within the expected range for a square planar $[CuN_2S_2]$ coordination environment,[63,64] and are similar to those measured for the parent CuATSM complex (also shown).[65] In particular, a quintet superhyperfine splitting pattern is observed in the 3400–3650 G region, giving a superhyperfine constant of A_N = 16 G. This feature, also supported by the g_{iso} value, reveals a significant covalent character for the Cu^{2+}–ligand interaction.[66] The incorporated ethylene glycol moieties have little effect on the symmetry of the CuN_2S_2 coordination core, leaving the two nitrogen-donating ligands indistinguishable as is true with the parent symmetric CuATSM complex.[65] These results further certify that our modifications to the CuATSM core do not perturb the copper coordination environment.

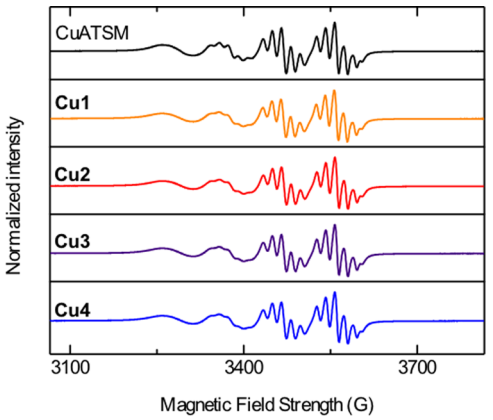

Figure 2. X-band EPR spectrum of CuATSM and **Cu1**–**4** in DMF solution at 298 K.

2.4. Lipophilicity. We evaluated the n-octanol/water partition coefficient log *P* ($\log(C_{octanol}/C_{water})$, where *C* = concentration) for **Cu1**–**4** as well as the nonfluorinated CuATSM according to Leo's method.[67] While the introduction of the perfluoro-*t*-butyl moiety increases the lipophilicity of the complexes, ethylene glycol linkers will have the opposite effect. Consistent with previous reports, the nonfluorinated CuATSM showed a mild lipophilicity (log *P* = 1.50). All of the synthesized CuATSM derivatives, **Cu1**–**4**, showed higher log *P* values from 1.65 to 2.87, which reflects the hydrophobic nature of the C–F bonds. On the other hand, a progressive decrease in log *P* values was observed with **Cu1**, **Cu2**, **Cu3**, and **Cu4** having values of 2.87, 2.53, 2.23, and 1.65, respectively. This validates that incorporation of hydrophilic ethylene glycol linkers significantly attenuates the lipophilicity of these complexes.

2.5. Cyclic Voltammetry. Hypoxia selectivity in this class of compounds is in part governed by their $Cu^{2+/+}$ reduction potential, with optimal selectivity demonstrated for CuATSM with an $E_{1/2}$ = −0.63 V versus SCE (measured in DMF), and no selectivity for compounds with $E_{1/2} \geq -0.50$ V.[60] In our previous work, incorporation of fluorine atoms five atoms away from the coordinating S atoms resulted in cathodic shifts in reduction potential, so much so that incorporation of two $-CF_3$ groups in this scaffold yielded a complex with $E_{1/2}$ = −0.49 V.[50] We hypothesized that increasing the distance between the fluorine tag and the Cu center should cause an anodic shift in reduction potential, rendering complexes with reduction potentials better tuned for hypoxia selectivity. As shown in Figure 3, in DMF solution, all four complexes displayed a (quasi)reversible peak for the $Cu^{2+/+}$ redox couple, with peak potential separations ranging from 80 to 127 mV. Incorporation of electron-withdrawing perfluorinated *tert*-butyl ether groups induced a slight cathodic shift of $E_{1/2}$ for Cu^{+}/Cu^{2+}, as seen in **Cu1** (−0.60 V) and **Cu2** (−0.61 V), but the effect was attenuated with an increase of the ethylene glycol chain length (−0.63 V for both **Cu3** and **Cu4**). The above reduction potentials indicate that complexes **Cu3** and **Cu4**, with sufficient separation between Cu^{2+} and fluorinated moieties, have optimal redox properties for hypoxia selectivity.

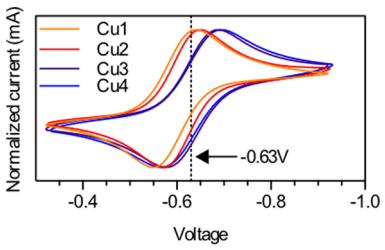

Figure 3. Cyclic voltammograms of **Cu1**–**4** (vs SCE) in DMF solution at 298 K.

2.6. ^{19}F NMR properties. The ^{19}F NMR spectra of the four ligands and corresponding Cu^{2+} complexes in d_6-DMSO revealed significant relaxation effects for all ethylene glycol chain lengths. A singlet peak at around −70.0 ppm was seen for all of the eight compounds, indicating that all appended fluorine atoms are in equivalent environments. Compared to the sharp peaks of free ligands **1**–**4** (half-height peak widths <10 Hz), the corresponding **Cu1**–**4** complexes displayed broader peaks with half-height peak widths ranging from 61 Hz for **Cu1** to 16 Hz for **Cu4** (Figure 4A). The fact that the Cu^{2+} center was able to strongly relax distant fluorine spins even in the **Cu4** is consistent with the long electronic relaxation time of the Cu^{2+} center, which leads to dramatic decreases in T_2 relaxation times of interacting nuclei. A table summarizing relevant NMR parameters for **1**–**4** and **Cu1**–**Cu4** is provided in the Supporting Information (Table S1).

The longitudinal (T_1) and transverse (T_2) relaxation times of both complexes and ligands were determined in DMSO (Figure 4B). For both the ligands and the complexes, increases in both

DOI: 10.1021/acs.inorgchem.7b00500
Inorg. Chem. XXXX, XXX, XXX–XXX

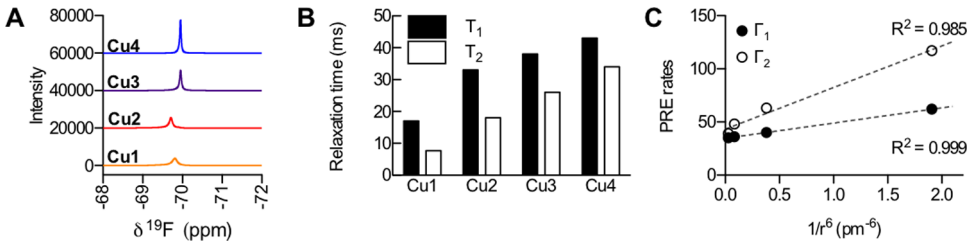

Figure 4. (A) ^{19}F NMR spectra of 20 mM **Cu1−4**. (B) Relaxation times (T_1, T_2) of 20 mM **Cu1−4**. (C) Linear fitting of longitudinal PRE rates (Γ_1) and transverse PRE rates (Γ_2) to the $1/r^6$ for **Cu1−4**. The R^2 value for the fitting are 0.999 and 0.985 for longitudinal PRE rates (Γ_1) and transverse PRE rates (Γ_2), respectively. NMR spectra and relaxation times were acquired at 298 K in d_6-DMSO at a field strength of 9.4 T.

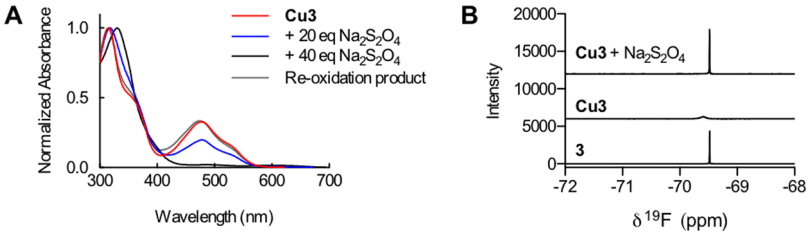

Figure 5. (A) UV−vis absorption changes by chemical reduction using $Na_2S_2O_4$. (B) ^{19}F NMR spectra illustrating the one-electron reduction of **Cu3** in a mixed solvent of 70% DMSO/20% HEPES buffer (pH 7.0, 20 mM)/10% D_2O using $Na_2S_2O_4$.

T_1 and T_2 were observed with an increase of the ethylene glycol chain length. For the free ligands, the T_1 increased from 1.06 s for **1** to 1.49 s for **4**, while T_2 increased from 0.90 s for **1** to 1.31 s for **4**. This enhancement was attributed to the improved flexibility of the fluorinated group as the length of the ethylene glycol chain linking it to the ATSM backbone increases. **Cu1−4** followed a similar trend for both T_1 (17−43 ms) and T_2 (7.7−34 ms). In addition to the enhanced flexibility of the fluorine-containing tail, the attenuated Cu^{2+} paramagnetic relaxation enhancement (PRE) effect likely contributes to the increasing relaxation times for the Cu complexes as the linker is extended. We calculated the ratio between the relaxation times of the ligands and corresponding Cu^{2+} complexes (T_n(ligand)/T_n(Cu complex), n = 1, 2). The results, described as longitudinal (Γ_1) and transverse (Γ_2) PRE rates, respectively, are shown in Figure 4C. Considering that Cu^{2+} only has one unpaired electron and a long electronic relaxation time, we assumed a major component of the PRE effect is through direct dipole−dipole interactions.[68] In this case, both longitudinal and transverse PRE rates are conventionally described by the Solomon−Bloembergen equations to give a proportional relationship between $\Gamma_{1,2}$ and $1/r^6$ (r is the distance between the metal center and the interacting nuclei).[69,70] Thus, by fitting the plot of Γ_1 and Γ_2 versus $1/r^6$ (r values estimated from DFT-optimized structures), we observed an approximate linear relationship (Figure 4C). We note that computational optimization cannot precisely predict the structure in solution phase in which fast conformational motions are expected, but can provide a means of estimating the maximum predicted distance between the Cu^{2+} center and the fluorinated spins. The above results suggest a regular pattern of PRE rates tuned by the distance between Cu^{2+} and F atoms, paving the way for future design of fluorinated CuATSM derivatives for ^{19}F PRE-based MR detection of hypoxia.

2.7. In Vitro Reduction Studies. To demonstrate the reduction of our fluorinated Cu(II)ATSM derivatives in reducing environments, we monitored the reduction of **Cu3** in vitro with UV−vis and NMR spectroscopies. By UV−vis, the initial DMF solution of **Cu3** exhibited an intense absorbance at 316 nm ($\varepsilon = 2.14 \times 10^4$ L mol^{-1} cm^{-1}) and a broad peak at 477 nm ($\varepsilon = 7.01 \times 10^3$ L mol^{-1} cm^{-1}) (Figure 5A). Titrating concentrated aqueous $Na_2S_2O_4$ into this solution rendered a red-shift of the sharp band at 311 nm, a dramatic quench of the absorbance band at 477 nm, and a slight increase of a broad band at ∼600 nm. Full disappearance of the peak at 477 nm was observed after addition of 40 equiv of $Na_2S_2O_4$. These absorbance changes are consistent with a metal-centered reduction as has been observed with similar complexes.[71] During titration, a small amount of water was added upon addition of $Na_2S_2O_4$. Thus, the observed product is likely a mixture of the anionic [**Cu(I)3**]$^-$ complex and the free ligand **3**, with the former being the major species. Back oxidation by air diffusion into the cuvette for 30 min recovered the broad peak at 477 nm, with the restored spectrum overlapping well with the initial.

The reduction was further monitored by ^{19}F NMR, which was performed in a mixture of 70% DMSO and 30% aqueous buffer (Figure 5B). Prior to reduction, **Cu3** showed a broad peak with a peak width at half-height of 38 Hz. This larger peak width relative to that observed in pure DMSO (21 Hz) is likely due to the increased water content in the solvent. After incubation of **Cu3** with $Na_2S_2O_4$ for 5 min, the ^{19}F NMR spectrum of the crude reaction revealed an intense singlet at δ = −69.5 ppm, which matched up well with the spectrum of ligand **3**. At this water concentration, the ligand has likely dissociated from the Cu(I), giving **3** as the major product. The transverse nuclear relaxation time T_2 was further measured. After the reduction, the system displayed a T_2 of 0.76 s, a 129-fold increase as compared to the T_2 of **Cu3** in the same solvent system. The corresponding peak intensity increased by 22-fold.

2.8. Stability, Cytotoxicity, and Cell Uptake. Prior to initiating cell experiments, we examined the stability of our CuATSM derivatives in cell-culture media using UV−vis spectroscopy. After leaving 30 μM solutions of complexes **Cu1−4** for 24 h, only small to negligible changes in absorbance were recorded (Figure S3) for **Cu2−4**, indicating their considerable stability in biological media. The absorbance peaks for **Cu1**, however, disappeared after 24 h incubation; we

DOI: 10.1021/acs.inorgchem.7b00500
Inorg. Chem. XXXX, XXX, XXX−XXX

attribute this to precipitation of the complex due to its low aqueous solubility. Indeed, visible precipitate was observed when aqueous solutions of this complex were left for 24 h. Thus, **Cu1** was deemed not suitable for further biological studies, and further cell experiments were performed solely with **Cu2−4**.

Cytotoxicity of **Cu2−4** was tested in a human breast cancer cell line (MCF-7) using a live/dead assay. Cells were treated with the three synthesized complexes, respectively, at a concentration of 30 μM for 4 h, and the cell viability was evaluated using the ReadyProbes Cell Viability Imaging Kit (blue/green). The results are compiled in Figures S4 and S5. In both normoxic (20% O_2) and hypoxic (0.1% O_2) environments, little fluorescence was recorded in the green channel for dead cell staining, revealing low cytotoxicity of the Cu^{2+} complexes (>98% viability for all Cu-treated cells, see Figure S6). Thus, at an incubation concentration of 30 μM Cu^{2+}-complex (270 μM fluorine concentration), the cell condition was ideal for further studies to differentiate hypoxic and normoxic cells using ^{19}F NMR/MRI-based detection.

Cellular uptake levels were investigated by treating MCF-7 cells with **Cu2−4** for 4 h and measuring the intracellular Cu content through ICP-OES, together with $CuCl_2$ as a control. The results are compiled in Figure 6. Compared to the $CuCl_2$

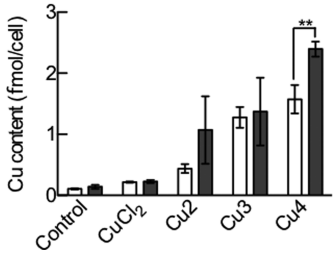

Figure 6. Uptake levels of **Cu2−4** in MCF-7 cells under both normoxic (20%, white bars) and hypoxic (0.1%, gray bars) conditions. MCF-7 cells were incubated with 30 μM Cu^{2+} complex for 4 h before the intracellular Cu content was analyzed by ICP-OES. The control group represents cells that were not incubated with a copper source. $CuCl_2$ (30 μM) was used as an additional control to demonstrate the effect of transportation of the complex into cells with incubation under the same conditions.

control group, improved cell uptake was observed for **Cu2−4** at femtomole levels per cell, suggesting that the synthesized ATSM derivatives are effective to transport Cu^{2+} into cells. Better cell uptake was seen with an increase of the ethylene glycol chain length under both normoxic (20% O_2) and hypoxic (0.1% O_2) conditions. Interestingly, the only complex that exhibited a significant increase in cell uptake under hypoxic conditions compared to normoxic conditions was **Cu4**, showing a 52% enhancement in cell uptake when grown under hypoxic conditions for 4 h. We note that, in a noncancerous cell type (HEK293 cells), no difference in cellular copper content was observed following incubation with **Cu4** under normoxic and hypoxic conditions.

2.9. MR Imaging and in Vitro NMR Studies. We used **4** and **Cu4** as representative compounds to demonstrate the application of fluorinated CuATSM derivatives for MR-based studies. A series of phantom images were acquired on a 7 T preclinical MRI system using a rapid acquisition with relaxation enhancement (RARE) sequence. Due to the short relaxation time of **Cu4**, a short echo pulse sequence, with TE (echo time) = 10 ms and TR (repetition time) = 100 ms, was used. In comparison, the slowly relaxing **4** was best imaged with a long echo pulse sequence employing TE = 100 ms and TR = 2040 ms. We determined the limit of detection (LOD) for **4** and **Cu4** at a total scan time of 2 h (Figure 7). Good linearity was achieved when plotting the signal-to-noise ratio (SNR) versus sample concentration for both **4** (r^2 = 0.996) and **Cu4** (r^2 = 0.996) (Figure 7B,D). The LOD was further evaluated from the fitted line by using a threshold of 3-fold of the SNR for the blank sample and was determined to be 0.44 mM for **4** (4.1 mM ^{19}F) and 0.099 mM for **Cu4** (0.89 mM ^{19}F). The LOD of **4** falls on the same scale as the previously reported values.[12,72] The paramagnetically relaxed ^{19}F MR signal (i.e., **Cu4**) showed a 4.5-fold increase in SNR due to the increased scan rate enabled by the short echo pulse sequence. This submillimolar probe detection limit holds great promise for future use of this class of probes in biological systems.

The large difference in relaxation times between **4** and **Cu4** allowed us to differentiate them through ^{19}F MRI. Figure 8A shows ^{19}F MR images of four tubes containing a solvent blank (DMSO), a 1 mM DMSO solution of **4**, a 1 mM DMSO solution of **Cu4**, and a mixed DMSO solution of 1 mM **4** and 1 mM **Cu4**. We scanned these samples using both the long and short echo sequences described above. As expected, the DMSO blank solution had zero detectable ^{19}F signal when either pulse sequence was used. When using the long echo sequence, the solution of **4** and the mixed solution of **Cu4** and **4** both gave a strong signal (SNR 16.0 and 16.4, respectively), while the **Cu4**-only solution signal was not above the detection threshold (SNR 2.0) as its magnetization relaxes before image acquisition begins. On the other hand, when using the short echo sequence, the opposite results were obtained. Bright signals were seen in the solutions containing **Cu4** (SNR 11.5 and 13.4 for the **Cu4**-only solution and solution mixture of **Cu4** and **4**, respectively). Only a negligible signal of **4** was detected (SNR 3.4), as very little diamagnetic species relaxes during the short echo pulse sequence time frame.

The efficient ^{19}F signal differentiation, combined with submillimolar detection limit for **4** and **Cu4**, prompted us to track the reduction of **Cu4** through ^{19}F MRI as a further step toward application (Figure 8B). **Cu4** (1 mM) was incubated with 2 equiv of $Na_2S_2O_4$ in a DMSO/HEPES (7/3, v/v) mixture for 5 min, where the reduction happened immediately, changing the solution color from reddish brown to bright yellow. With application of the long echo pulse sequence, an increased signal was detected. Analysis of the SNR gave a signal enhancement of 6.1-fold upon reduction of the Cu^{2+} complex. However, when using the short echo pulse sequence, only negligible signal was recorded (SNR 1.8), indicating an almost complete reduction of **Cu4**. Taken together, the above results suggest that ^{19}F MRI can be used to track both the ligand and its Cu^{2+} complex and monitor hypoxia-based reduction events.

We finally used ^{19}F NMR to test the potential for **Cu4** to differentiate cells cultured in normoxic (20% O_2) and hypoxic (0.1% O_2) conditions. MCF-7 cells were incubated with 30 μM **Cu4** for 4 h under hypoxic and normoxic conditions, and whole cell suspensions were transferred to NMR tubes under the same oxygen levels. We also mixed cell-culture media with 30 μM **Cu4** and used it as a cell-free control. The results are compiled in Figure 8C. While there was almost negligible ^{19}F NMR signal (SNR 4.7 compared to the calculated spectral noise level) observed in the cell-free control group, a ^{19}F signal increase at δ = −70.5 ppm in the hypoxic group (SNR 22.4)

DOI: 10.1021/acs.inorgchem.7b00500
Inorg. Chem. XXXX, XXX, XXX−XXX

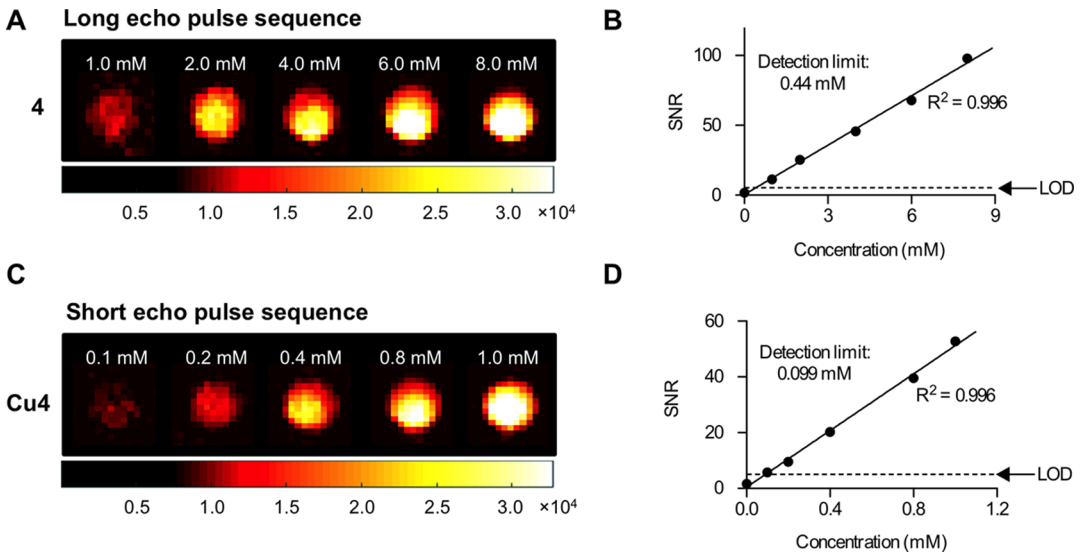

Figure 7. Determination of LOD on **4** and **Cu4** through ^{19}F MRI at a field of 7.0 T at 22 °C. (A, C) ^{19}F MRI performed on phantoms containing **4** (A) or **Cu4** (C) diluted in DMSO at different concentrations. (B, D) Linearity of signal-to-noise ratio (SNR) versus concentration of **4** (A) or **Cu4** (C), together with a SNR threshold for the detection limit. A long echo pulse sequence was used for **4** (TE = 100 ms, TR = 2040 ms), and a short echo pulse sequence was used for **Cu4** (TE = 10 ms, TR = 100 ms).

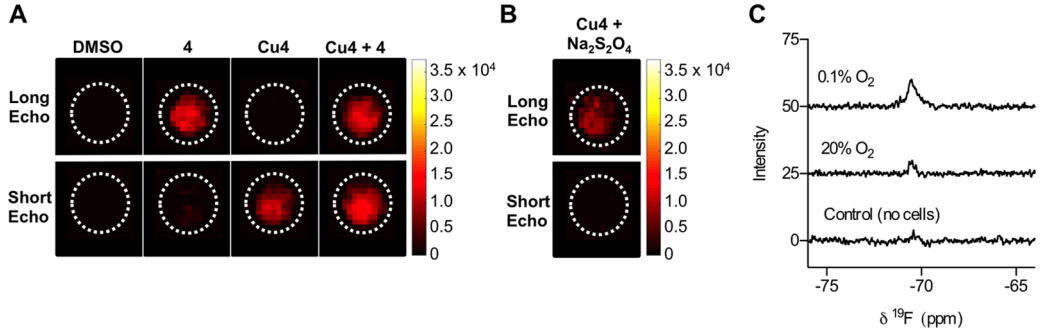

Figure 8. Differentiation of **Cu4** and **4** through long and short echo ^{19}F MR pulse sequences at a field of 7.0 T at 22 °C. (A) ^{19}F MR images of solvent blank (left column) and DMSO solutions containing 1 mM **4** (2nd-left column), 1 mM **Cu4** (2nd-right column), and 1 mM **Cu4** plus 1 mM **4** (right column). (B) ^{19}F MR images of in vitro reduction of **Cu4** by using 2 equiv of $Na_2S_2O_4$ in a DMSO/HEPES (7/3, v/v) mixture. Top row for parts A and B: long echo pulse sequence was used, TE = 100 ms, TR = 2040 ms, 588 scans (~2 h). Bottom row for parts A and B: short echo pulse sequence was used, TE = 10 ms, TR = 100 ms, 588 scans (~6 min). (C) ^{19}F NMR spectra at 11.7 T of live MCF-7 cells using **Cu4** demonstrating increased signal intensity under hypoxic conditions (0.1% O_2), together with cell-culture media mixed with 30 μM **Cu4** as a cell-free control.

was observed, suggesting an efficient reduction of the complex by the cellular machinery. On the other hand, only a weak signal was observed for the normoxic group (SNR 8.2), which we ascribe mainly to a limited reduction of the complex inside cells in the normoxic environment and, in part, from the signal of **Cu4** itself. With the above results suggesting a potential for this class of compounds to act as reporters to track hypoxic cells using ^{19}F MRI, future work will focus on introducing groups to improve the water solubility and fluorine content of the molecule to enable in cell and in vivo MR imaging of hypoxia.

3. CONCLUSION

In conclusion, we have synthesized a series of CuATSM derivatives that bear nine identical fluorine atoms and a variable-length ethylene glycol linker between the ATSM backbone and the fluorinated tag. Attaching ethylene-glycol-linked fluorine groups to the CuATSM framework maintained the coordination geometry of the Cu^{2+} center and rendered the redox behavior of the new complexes similar to that of CuATSM despite the presence of electron-withdrawing functionalities. The PRE effect of Cu^{2+} in fluorinated CuATSM derivatives was quantitatively studied for the first time, exhibiting a T_2-increase of 129-fold between one of the Cu^{2+} complexes and its reduced system. Applying the transverse PRE rates of the complex to the theoretical model of PRE through a dipole−dipole interaction demonstrated a regular pattern for the PRE effect through space tuning, with a $1/r^6$ dependence. We note that there is significant relaxation enhancement even when the fluorine tag is positioned ~18 Å away from the $S = {}^1/_2$ Cu^{2+} center, opening up a number of possibilities for next generation probes. Introducing an ethylene glycol linker effectively modulates the lipophilicity and redox properties of the complexes, leading to different cell uptake levels and selectivity between cells grown under normoxic and hypoxic conditions. MR phantom images were collected using **4** and **Cu4** as representatives and demonstrated efficient differentiation of ^{19}F nuclei from the complex versus the ligand through two different RARE pulse sequences. The ^{19}F spin density detection limits were further determined to be 0.44 mM for the ligand and 0.099 mM for the complex using their

DOI: 10.1021/acs.inorgchem.7b00500
Inorg. Chem. XXXX, XXX, XXX−XXX

optimized imaging pulse sequences. Further, we tracked ^{19}F signal changes upon reduction of **Cu4** both chemically and in the hypoxic cellular environment through MRI and NMR. Ongoing work in this system is focused on optimization of cell uptake levels as well as further enhancement of both fluorine spin density and water solubility. Further, the reported imaging results in which short echo sequences enable detection of fluorinated Cu^{2+} species provide an intriguing avenue for the development of new imaging agents.

■ ASSOCIATED CONTENT

Supporting Information

The Supporting Information is available free of charge on the ACS Publications website at DOI: 10.1021/acs.inorgchem.7b00500.

Details about syntheses and other methods, and supplementary data files (PDF)

Accession Codes

CCDC 1549916 contains the supplementary crystallographic data for this paper. These data can be obtained free of charge via www.ccdc.cam.ac.uk/data_request/cif, or by emailing data_request@ccdc.cam.ac.uk, or by contacting The Cambridge Crystallographic Data Centre, 12 Union Road, Cambridge CB2 1EZ, UK; fax: +44 1223 336033.

■ AUTHOR INFORMATION

Corresponding Author

*E-mail: emilyque@cm.utexas.edu.

ORCID

Emily L. Que: 0000-0001-6604-3052

Author Contributions

The manuscript was written through contributions of all authors. All authors have given approval to the final version of the manuscript.

Funding

This work was supported by start-up funds from the University of Texas at Austin, the Welch Foundation (F-1883), a University of Texas at Austin Undergraduate Research grant (V.K.), and a University of Texas at Austin Graduate School Summer Fellowship (D.X.).

Notes

The authors declare no competing financial interest.

■ ACKNOWLEDGMENTS

We thank Dr. Vincent Lynch for X-ray crystallography support and Dr. Bradley Holliday for providing access to Gaussian. We also acknowledge the Imaging Research Center at UT—Austin for access to their facilities.

■ REFERENCES

(1) Vaupel, P.; Mayer, A.; Höckel, M. In *Methods in Enzymology*; Academic Press, 2004; Vol. *381*, pp 335−354.

(2) Wilson, W. R.; Hay, M. P. Targeting hypoxia in cancer therapy. *Nat. Rev. Cancer* **2011**, *11*, 393−410.

(3) Padhani, A. R.; Krohn, K. A.; Lewis, J. S.; Alber, M. Imaging oxygenation of human tumours. *Eur. Radiol.* **2007**, *17*, 861−872.

(4) Gillies, R. J.; Gatenby, R. A. Hypoxia and adaptive landscapes in the evolution of carcinogenesis. *Cancer Metastasis Rev.* **2007**, *26*, 311−317.

(5) Pacheco-Torres, J.; López-Larrubia, P.; Ballesteros, P.; Cerdán, S. Imaging tumor hypoxia by magnetic resonance methods. *NMR Biomed.* **2011**, *24*, 1−16.

(6) Di Gregorio, E.; Ferrauto, G.; Gianolio, E.; Lanzardo, S.; Carrera, C.; Fedeli, F.; Aime, S. An MRI Method To Map Tumor Hypoxia Using Red Blood Cells Loaded with a pO_2-Responsive Gd-Agent. *ACS Nano* **2015**, *9*, 8239−8248.

(7) Gulaka, P. K.; Rojas-Quijano, F.; Kovacs, Z.; Mason, R. P.; Sherry, A. D.; Kodibagkar, V. D. $GdDO_3NI$, a nitroimidazole-based T_1 MRI contrast agent for imaging tumor hypoxia in vivo. *JBIC, J. Biol. Inorg. Chem.* **2014**, *19*, 271−279.

(8) Ratnakar, S. J.; Soesbe, T. C.; Lumata, L. L.; Do, Q. N.; Viswanathan, S.; Lin, C.-Y.; Sherry, A. D.; Kovacs, Z. Modulation of CEST Images in Vivo by T_1 Relaxation: A New Approach in the Design of Responsive PARACEST Agents. *J. Am. Chem. Soc.* **2013**, *135*, 14904−14907.

(9) Rojas-Quijano, F. A.; Tircsó, G.; Tircsóné Benyó, E.; Baranyai, Z.; Tran Hoang, H.; Kálmán, F. K.; Gulaka, P. K.; Kodibagkar, V. D.; Aime, S.; Kovács, Z.; Sherry, A. D. Synthesis and Characterization of a Hypoxia-Sensitive MRI Probe. *Chem. - Eur. J.* **2012**, *18*, 9669−9676.

(10) Tanabe, K.; Harada, H.; Narazaki, M.; Tanaka, K.; Inafuku, K.; Komatsu, H.; Ito, T.; Yamada, H.; Chujo, Y.; Matsuda, T.; Hiraoka, M.; Nishimoto, S.-i. Monitoring of Biological One-Electron Reduction by ^{19}F NMR Using Hypoxia Selective Activation of an ^{19}F-Labeled Indolequinone Derivative. *J. Am. Chem. Soc.* **2009**, *131*, 15982−15983.

(11) Liu, S.; Shah, S. J.; Wilmes, L. J.; Feiner, J.; Kodibagkar, V. D.; Wendland, M. F.; Mason, R. P.; Hylton, N.; Hopf, H. W.; Rollins, M. D. Quantitative tissue oxygen measurement in multiple organs using ^{19}F MRI in a rat model. *Magn. Reson. Med.* **2011**, *66*, 1722−1730.

(12) Yu, J.-x.; Kodibagkar, V.; Cui, W.; Mason, R. 19F: A Versatile Reporter for Non-Invasive Physiology and Pharmacology Using Magnetic Resonance. *Curr. Med. Chem.* **2005**, *12*, 819−848.

(13) Lu, M.; Zhu, X.-H.; Zhang, Y.; Chen, W. Intracellular redox state revealed by in vivo ^{31}P MRS measurement of NAD^+ and NADH contents in brains. *Magn. Reson. Med.* **2014**, *71*, 1959−1972.

(14) Keshari, K. R.; Kurhanewicz, J.; Bok, R.; Larson, P. E. Z.; Vigneron, D. B.; Wilson, D. M. Hyperpolarized ^{13}C dehydroascorbate as an endogenous redox sensor for in vivo metabolic imaging. *Proc. Natl. Acad. Sci. U. S. A.* **2011**, *108*, 18606−18611.

(15) Bohndiek, S. E.; Kettunen, M. I.; Hu, D.-e.; Kennedy, B. W. C.; Boren, J.; Gallagher, F. A.; Brindle, K. M. Hyperpolarized [1-^{13}C]-Ascorbic and Dehydroascorbic Acid: Vitamin C as a Probe for Imaging Redox Status in Vivo. *J. Am. Chem. Soc.* **2011**, *133*, 11795−11801.

(16) Barskiy, D. A.; Shchepin, R. V.; Coffey, A. M.; Theis, T.; Warren, W. S.; Goodson, B. M.; Chekmenev, E. Y. Over 20% ^{15}N Hyperpolarization in Under One Minute for Metronidazole, an Antibiotic and Hypoxia Probe. *J. Am. Chem. Soc.* **2016**, *138*, 8080−8083.

(17) Do, Q. N.; Ratnakar, J. S.; Kovács, Z.; Sherry, A. D. Redox- and Hypoxia-Responsive MRI Contrast Agents. *ChemMedChem* **2014**, *9*, 1116−1129.

(18) Iwaki, S.; Hanaoka, K.; Piao, W.; Komatsu, T.; Ueno, T.; Terai, T.; Nagano, T. Development of hypoxia-sensitive Gd^{3+}-based MRI contrast agents. *Bioorg. Med. Chem. Lett.* **2012**, *22*, 2798−2802.

(19) Takahashi, S.; Piao, W.; Matsumura, Y.; Komatsu, T.; Ueno, T.; Terai, T.; Kamachi, T.; Kohno, M.; Nagano, T.; Hanaoka, K. Reversible Off−On Fluorescence Probe for Hypoxia and Imaging of Hypoxia−Normoxia Cycles in Live Cells. *J. Am. Chem. Soc.* **2012**, *134*, 19588−19591.

(20) Kiyose, K.; Hanaoka, K.; Oushiki, D.; Nakamura, T.; Kajimura, M.; Suematsu, M.; Nishimatsu, H.; Yamane, T.; Terai, T.; Hirata, Y.; Nagano, T. Hypoxia-Sensitive Fluorescent Probes for in Vivo Real-Time Fluorescence Imaging of Acute Ischemia. *J. Am. Chem. Soc.* **2010**, *132*, 15846−15848.

(21) Li, Y.; Sun, Y.; Li, J.; Su, Q.; Yuan, W.; Dai, Y.; Han, C.; Wang, Q.; Feng, W.; Li, F. Ultrasensitive Near-Infrared Fluorescence-Enhanced Probe for in Vivo Nitroreductase Imaging. *J. Am. Chem. Soc.* **2015**, *137*, 6407−6416.

(22) Yang, D. J.; Wallace, S.; Cherif, A.; Li, C.; Gretzer, M. B.; Kim, E. E.; Podoloff, D. A. Development of F-18-labeled fluoroerythronitroimidazole as a PET agent for imaging tumor hypoxia. *Radiology* **1995**, *194*, 795−800.

DOI: 10.1021/acs.inorgchem.7b00500
Inorg. Chem. XXXX, XXX, XXX−XXX

(23) Lopci, E.; Grassi, I.; Chiti, A.; Nanni, C.; Cicoria, G.; Toschi, L.; Fonti, C.; Lodi, F.; Mattioli, S.; Fanti, S. PET radiopharmaceuticals for imaging of tumor hypoxia: a review of the evidence. *Am. J. Nucl. Med. Mol. Imaging* **2014**, *4*, 365−384.
(24) Ruiz-Cabello, J.; Barnett, B. P.; Bottomley, P. A.; Bulte, J. W. M. Fluorine ((19)F) MRS and MRI in biomedicine. *NMR Biomed.* **2011**, *24*, 114−129.
(25) Srinivas, M.; Boehm-Sturm, P.; Figdor, C. G.; de Vries, I. J.; Hoehn, M. Labeling cells for in vivo tracking using 19F MRI. *Biomaterials* **2012**, *33*, 8830−8840.
(26) Tirotta, I.; Dichiarante, V.; Pigliacelli, C.; Cavallo, G.; Terraneo, G.; Bombelli, F. B.; Metrangolo, P.; Resnati, G. 19F Magnetic Resonance Imaging (MRI): From Design of Materials to Clinical Applications. *Chem. Rev.* **2015**, *115*, 1106−1129.
(27) Ahrens, E. T.; Flores, R.; Xu, H.; Morel, P. A. In vivo imaging platform for tracking immunotherapeutic cells. *Nat. Biotechnol.* **2005**, *23*, 983−987.
(28) Janjic, J. M.; Srinivas, M.; Kadayakkara, D. K. K.; Ahrens, E. T. Self-delivering Nanoemulsions for Dual Fluorine-19 MRI and Fluorescence Detection. *J. Am. Chem. Soc.* **2008**, *130*, 2832−2841.
(29) Zhao, D.; Jiang, L.; Mason, P. R. In *Methods in Enzymology*; Academic Press, 2004; Vol. *386*, pp 378−418.
(30) Barandov, A.; Bartelle, B. B.; Gonzalez, B. A.; White, W. L.; Lippard, S. J.; Jasanoff, A. Complexes for Molecular Magnetic Resonance Imaging of Intracellular Targets. *J. Am. Chem. Soc.* **2016**, *138*, 5483−5486.
(31) Jeon, I.-R.; Park, J. G.; Haney, C. R.; Harris, T. D. Spin crossover iron(ii) complexes as PARACEST MRI thermometers. *Chem. Sci.* **2014**, *5*, 2461−2465.
(32) Du, K.; Harris, T. D. A $Cu(II)_2$ Paramagnetic Chemical Exchange Saturation Transfer Contrast Agent Enabled by Magnetic Exchange Coupling. *J. Am. Chem. Soc.* **2016**, *138*, 7804−7807.
(33) Harvey, P.; Kuprov, I.; Parker, D. Lanthanide Complexes as Paramagnetic Probes for ^{19}F Magnetic Resonance. *Eur. J. Inorg. Chem.* **2012**, *2012*, 2015−2022.
(34) Gale, E. M.; Atanasova, I. P.; Blasi, F.; Ay, I.; Caravan, P. A Manganese Alternative to Gadolinium for MRI Contrast. *J. Am. Chem. Soc.* **2015**, *137*, 15548−15557.
(35) Gale, E. M.; Jones, C. M.; Ramsay, I.; Farrar, C. T.; Caravan, P. A Janus Chelator Enables Biochemically Responsive MRI Contrast with Exceptional Dynamic Range. *J. Am. Chem. Soc.* **2016**, *138*, 15861−15864.
(36) Dorazio, S. J.; Tsitovich, P. B.; Siters, K. E.; Spernyak, J. A.; Morrow, J. R. Iron(II) PARACEST MRI Contrast Agents. *J. Am. Chem. Soc.* **2011**, *133*, 14154−14156.
(37) Olatunde, A. O.; Dorazio, S. J.; Spernyak, J. A.; Morrow, J. R. The NiCEST Approach: Nickel(II) ParaCEST MRI Contrast Agents. *J. Am. Chem. Soc.* **2012**, *134*, 18503−18505.
(38) Mizukami, S.; Takikawa, R.; Sugihara, F.; Shirakawa, M.; Kikuchi, K. Dual-Function Probe to Detect Protease Activity for Fluorescence Measurement and ^{19}F MRI. *Angew. Chem., Int. Ed.* **2009**, *48*, 3641−3643.
(39) Mizukami, S.; Takikawa, R.; Sugihara, F.; Hori, Y.; Tochio, H.; Wälchli, M.; Shirakawa, M.; Kikuchi, K. Paramagnetic Relaxation-Based ^{19}F MRI Probe To Detect Protease Activity. *J. Am. Chem. Soc.* **2008**, *130*, 794−795.
(40) Ekanger, L. A.; Polin, L. A.; Shen, Y.; Haacke, E. M.; Martin, P. D.; Allen, M. J. A Eu^{II}-Containing Cryptate as a Redox Sensor in Magnetic Resonance Imaging of Living Tissue. *Angew. Chem., Int. Ed.* **2015**, *54*, 14398−14401.
(41) Ekanger, L. A.; Allen, M. J. Overcoming the concentration-dependence of responsive probes for magnetic resonance imaging. *Metallomics* **2015**, *7*, 405−421.
(42) Harrison, V. S. R.; Carney, C. E.; MacRenaris, K. W.; Waters, E. A.; Meade, T. J. Multimeric Near IR−MR Contrast Agent for Multimodal In Vivo Imaging. *J. Am. Chem. Soc.* **2015**, *137*, 9108−9116.
(43) Major, J. L.; Parigi, G.; Luchinat, C.; Meade, T. J. The synthesis and in vitro testing of a zinc-activated MRI contrast agent. *Proc. Natl. Acad. Sci. U. S. A.* **2007**, *104*, 13881−13886.
(44) Haedicke, I. E.; Li, T.; Zhu, Y. L. K.; Martinez, F.; Hamilton, A. M.; Murrell, D. H.; Nofiele, J. T.; Cheng, H.-L. M.; Scholl, T. J.; Foster, P. J.; Zhang, X.-a. An enzyme-activatable and cell-permeable Mn^{III}-porphyrin as a highly efficient T_1 MRI contrast agent for cell labeling. *Chem. Sci.* **2016**, *7*, 4308−4317.
(45) Zhang, S.; Trokowski, R.; Sherry, A. D. A Paramagnetic CEST Agent for Imaging Glucose by MRI. *J. Am. Chem. Soc.* **2003**, *125*, 15288−15289.
(46) Aime, S.; Delli Castelli, D.; Fedeli, F.; Terreno, E. A Paramagnetic MRI-CEST Agent Responsive to Lactate Concentration. *J. Am. Chem. Soc.* **2002**, *124*, 9364−9365.
(47) Wu, Y.; Zhou, Y.; Ouari, O.; Woods, M.; Zhao, P.; Soesbe, T. C.; Kiefer, G. E.; Sherry, A. D. Polymeric PARACEST Agents for Enhancing MRI Contrast Sensitivity. *J. Am. Chem. Soc.* **2008**, *130*, 13854−13855.
(48) Yu, M.; Ambrose, S. L.; Whaley, Z. L.; Fan, S.; Gorden, J. D.; Beyers, R. J.; Schwartz, D. D.; Goldsmith, C. R. A Mononuclear Manganese(II) Complex Demonstrates a Strategy To Simultaneously Image and Treat Oxidative Stress. *J. Am. Chem. Soc.* **2014**, *136*, 12836−12839.
(49) Senanayake, P. K.; Rogers, N. J.; Finney, K.-L. N. A.; Harvey, P.; Funk, A. M.; Wilson, J. I.; O'Hogain, D.; Maxwell, R.; Parker, D.; Blamire, A. M. A new paramagnetically shifted imaging probe for MRI. *Magn. Reson. Med.* **2017**, *77*, 1307−1317.
(50) Xie, D.; King, T. L.; Banerjee, A.; Kohli, V.; Que, E. L. Exploiting Copper Redox for ^{19}F Magnetic Resonance-Based Detection of Cellular Hypoxia. *J. Am. Chem. Soc.* **2016**, *138*, 2937−2940.
(51) Chalmers, K. H.; De Luca, E.; Hogg, N. H. M.; Kenwright, A. M.; Kuprov, I.; Parker, D.; Botta, M.; Wilson, J. I.; Blamire, A. M. Design Principles and Theory of Paramagnetic Fluorine-Labelled Lanthanide Complexes as Probes for 19F Magnetic Resonance: A Proof-of-Concept Study. *Chem. - Eur. J.* **2010**, *16*, 134−148.
(52) Schmid, F.; Höltke, C.; Parker, D.; Faber, C. Boosting 19F MRI—SNR efficient detection of paramagnetic contrast agents using ultrafast sequences. *Magn. Reson. Med.* **2013**, *69*, 1056−1062.
(53) De Luca, E.; Harvey, P.; Chalmers, K. H.; Mishra, A.; Senanayake, P. K.; Wilson, J. I.; Botta, M.; Fekete, M.; Blamire, A. M.; Parker, D. Characterisation and evaluation of paramagnetic fluorine labelled glycol chitosan conjugates for 19F and 1H magnetic resonance imaging. *JBIC, J. Biol. Inorg. Chem.* **2014**, *19*, 215−227.
(54) Srivastava, K.; Weitz, E. A.; Peterson, K. L.; Marjańska, M.; Pierre, V. C. Fe- and Ln-DOTAm-F12 Are Effective Paramagnetic Fluorine Contrast Agents for MRI in Water and Blood. *Inorg. Chem.* **2017**, *56*, 1546−1557.
(55) Kislukhin, A. A.; Xu, H.; Adams, S. R.; Narsinh, K. H.; Tsien, R. Y.; Ahrens, E. T. Paramagnetic fluorinated nanoemulsions for sensitive cellular fluorine-19 magnetic resonance imaging. *Nat. Mater.* **2016**, *15*, 662−668.
(56) van Eldik, R.; Bertini, I. *Advances in Inorganic Chemistry: Relaxometry of Water-Metal Ion Interactions*; Elsevier Science, 2005.
(57) Bertini, I.; Turano, P.; Vila, A. J. Nuclear magnetic resonance of paramagnetic metalloproteins. *Chem. Rev.* **1993**, *93*, 2833−2932.
(58) Bertini, I.; Luchinat, C.; Parigi, G.; Ravera, E. In *NMR of Paramagnetic Molecules*, 2nd ed.; Elsevier: Boston, 2017; pp 77−126.
(59) Jahnke, W. In *BioNMR in Drug Research*; Wiley-VCH Verlag GmbH & Co. KGaA, 2003; pp 341−354.
(60) Dearling, J. L.; Lewis, J. S.; Mullen, G. E.; Welch, M. J.; Blower, P. J. Copper bis(thiosemicarbazone) complexes as hypoxia imaging agents: structure-activity relationships. *JBIC, J. Biol. Inorg. Chem.* **2002**, *7*, 249−259.
(61) Paterson, B. M.; Karas, J. A.; Scanlon, D. B.; White, J. M.; Donnelly, P. S. Versatile New Bis(thiosemicarbazone) Bifunctional Chelators: Synthesis, Conjugation to Bombesin(7−14)-NH_2, and Copper-64 Radiolabeling. *Inorg. Chem.* **2010**, *49*, 1884−1893.
(62) Cowley, A. R.; Dilworth, J. R.; Donnelly, P. S.; Labisbal, E.; Sousa, A. An Unusual Dimeric Structure of a Cu(I) Bis-(thiosemicarbazone) Complex: Implications for the Mechanism of

DOI: 10.1021/acs.inorgchem.7b00500
Inorg. Chem. XXXX, XXX, XXX−XXX

Hypoxic Selectivity of the Cu(II) Derivatives. *J. Am. Chem. Soc.* **2002**, *124*, 5270−5271.
(63) Peisach, J.; Blumberg, W. E. Structural implications derived from the analysis of electron paramagnetic resonance spectra of natural and artificial copper proteins. *Arch. Biochem. Biophys.* **1974**, *165*, 691−708.
(64) Sakaguchi, U.; Addison, A. W. Spectroscopic and redox studies of some copper(II) complexes with biomimetic donor atoms: implications for protein copper centres. *J. Chem. Soc., Dalton Trans.* **1979**, 600−608.
(65) West, D. X.; Ives, J. S.; Bain, G. A.; Liberta, A. E.; Valdés-Martínez, J.; Ebert, K. H.; Hernández-Ortega, S. Copper(II) and nickel(II) complexes of 2,3-butanedione bis(N(3)-substituted thiosemicarbazones). *Polyhedron* **1997**, *16*, 1895−1905.
(66) Holland, J. P.; Barnard, P. J.; Collison, D.; Dilworth, J. R.; Edge, R.; Green, J. C.; McInnes, E. J. L. Spectroelectrochemical and Computational Studies on the Mechanism of Hypoxia Selectivity of Copper Radiopharmaceuticals. *Chem. - Eur. J.* **2008**, *14*, 5890−5907.
(67) Leo, A.; Hansch, C.; Elkins, D. Partition coefficients and their uses. *Chem. Rev.* **1971**, *71*, 525−616.
(68) Clore, G. M.; Iwahara, J. Theory, Practice, and Applications of Paramagnetic Relaxation Enhancement for the Characterization of Transient Low-Population States of Biological Macromolecules and Their Complexes. *Chem. Rev.* **2009**, *109*, 4108−4139.
(69) Solomon, I. Relaxation Processes in a System of Two Spins. *Phys. Rev.* **1955**, *99*, 559−565.
(70) Bloembergen, N.; Morgan, L. O. Proton Relaxation Times in Paramagnetic Solutions. Effects of Electron Spin Relaxation. *J. Chem. Phys.* **1961**, *34*, 842−850.
(71) Holland, J. P.; Green, J. C.; Dilworth, J. R. Probing the mechanism of hypoxia selectivity of copper bis(thiosemicarbazonato) complexes: DFT calculation of redox potentials and absolute acidities in solution. *Dalton Trans.* **2006**, 783−794.
(72) Tirotta, I.; Mastropietro, A.; Cordiglieri, C.; Gazzera, L.; Baggi, F.; Baselli, G.; Bruzzone, M. G.; Zucca, I.; Cavallo, G.; Terraneo, G.; Baldelli Bombelli, F.; Metrangolo, P.; Resnati, G. A Superfluorinated Molecular Probe for Highly Sensitive in Vivo ^{19}F-MRI. *J. Am. Chem. Soc.* **2014**, *136*, 8524−8527.

DOI: 10.1021/acs.inorgchem.7b00500
Inorg. Chem. XXXX, XXX, XXX−XXX